Mechanical Systems and Signal Processing 224 (2025) 112140

Contents lists available at ScienceDirect

Mechanical Systems and Signal Processing

journal homepage: www.elsevier.com/locate/ymssp

Invited for the special issue in honor of Professor John Mottershead

A fast Time-domain identification of bushing dynamics

Francesco Cosco [a,*], Lorenzo Della Siega [b,c], Rocco Adduci [a], Paolo Gardonio [b], Wim Desmet [c,d], Domenico Mundo [a]

[a] University of Calabria, Mechanical, Energy and Management Engineering, Rende, Italy
[b] University of Udine, Dipartimento Politecnico di Ingegneria e Architettura, Udine, Italy
[c] KU Leuven, Mechanical Engineering, Leuven, Belgium
[d] Flanders Make@KU Leuven, Leuven, Belgium

ARTICLE INFO

Communicated by M. Krack

Keywords:
Bushing identification
DMA testing
Time-domain parameter identification

ABSTRACT

The identification of bushings dynamics is crucial for the development of innovative model-based digital tools, such as for example predictive maintenance or virtual sensing. Quite a few nonlinear modelling techniques have been proposed over the years, which can be suitably used to develop advanced models that capture the linear and nonlinear dynamics of a vast range of mechanical components and materials. Despite this, the experimental identification of bushings dynamics is usually accomplished with the so-called Dynamic Mechanical Analysis (DMA). This technique involves complex measurements based on several time-harmonic tests with different frequencies and amplitudes.

This paper proposes a cost-effective time-domain technique for the identification of the non-linear dynamics of bushing elements. A single-test approach is proposed, which significantly cuts the measurement time, but also simplifies the measurement procedure. The proposed identification method is validated experimentally with respect to the frequency-domain DMA-based approach. The parameters of three models, having incremental complexity, are identified using both approaches. Also, three validation tests are used to quantify the accuracy of the proposed approach. The results presented in this paper indicate that, irrespective of the model complexity, the dynamic response of the bushing models identified using the proposed time-domain approach is generally more accurate than those built with the classical DMA-based procedures, particularly for simple models.

1. Introduction

Rubber bushings are extensively used in mechanical systems to dampen the transmission of vibrations between components, particularly in applications involving large reversible deformations and loads such as the suspension system of cars, or the engine mounts. Normally, bushings are made of carbon-black filled rubber, or equivalent rubber-like materials [1], which are shaped into customised geometries, depending on the target application. In general, the dynamic response of bushings exhibits highly nonlinear characteristics, which depend on frequency and amplitude of the vibration disturbance, on the mounting preload and on the operation temperature [2,3]. Moreover, the hysteretic restoring force exerted by bushing components depends not only on the instantaneous deformation states, such as the imposed elongation and elongation rate, but also on the time history of the deformation itself [4].

* Corresponding author.
E-mail address: francesco.cosco@unical.it (F. Cosco).

https://doi.org/10.1016/j.ymssp.2024.112140
Received 15 May 2024; Received in revised form 26 September 2024; Accepted 8 November 2024

The development of accurate models of mechanical systems encompassing bushing components is of paramount importance for the development of advanced digital tools, such as for example predictive maintenance and virtual sensing, which are increasingly used to monitor and to control the functioning of mechanical systems, both off-line and on-line [5]. Several modelling strategies have emerged recently, which take into account the large variety of practical applications and the wide range of bushing designs. In this respect, the so-called modular modelling strategy [6,7], indicated also as the overlay approach [5], is proving very successful, particularly in developing simple, but effective, nonlinear lumped parameter models, which can be selected to comply with the complexity of the mechanical system at hand and to satisfy the required level of accuracy.

The effective identification of rubber bushing parameters is crucial to build models that predict accurately all aspects of their nonlinear behaviour, such as the dynamic stiffness and the loss factor, under different loading conditions. Therefore, to capture the whole nonlinear response of bushings, classical system identification approaches are employed, which comprise a set of static, quasi-static and dynamic (time-harmonic) tests implemented with different vibration amplitudes and frequencies [8]. For example, having considered the different aspects of the nonlinear dynamic responses of bushings, Dzierżek [9] suggested to run multiple tests, including (a) stepped harmonic excitation tests with the frequency ranging up to 100 Hz, (b) step input tests with varying amplitudes, and (c) triangular wave tests in the low frequency range.

Irrespective of the bulk of models presented in the literature, the identification of rubber bushings dynamic responses has converged towards the Dynamic Mechanical Analysis (DMA) [2,3,10]. This is a well-established approach, which consists in collecting the force response exerted by the bushing sample to a set of imposed time-harmonic displacements with a dedicated uni-axial test-machine, after reaching steady-state conditions. Indeed, the identification of rubber bushings mechanical properties is generally aimed at fitting the dynamic stiffness and loss factor of the bushing under different loading conditions, which are usually obtained from post-processing the information collected during the stepped-swept sine tests conducted over multiple frequencies and amplitudes. In this context, Li et al. [11] developed a back-propagation neural network to specifically predict the dynamic stiffness and loss factor of rubber bushings. Also, Zhang and Zhang [12] considered viscoelastic parameter identification based on structure-thermal analysis of rubber bushings, which relies on DMA experiments and on a novel approach for estimating hysteresis damping. Finally, Cosco et al. [7] presented an innovative approach combining a parameterisation technique with a nonlinear fitting optimisation algorithm, which has proven very accurate and efficient for the identification of rubber bushing mechanical parameters.

As recently discussed in [10], the classical frequency-domain parameter identification based on DMA requires expensive and time-consuming tests, which involve several time-harmonic analyses at steady-state conditions. Moreover, the outputs from the experimental measurements are normally condensed into dynamic stiffness and loss factor curves, which could lead to errors, as these curves may mask deviations from the assumed harmonic response. In this respect, for an effective parameter identification of complex nonlinear systems, it would be desirable to have a procedure that does not rely on data from stationary responses only. On the contrary, it would be preferable to have a methodology based on transient vibration tests with variable amplitudes, which would allow the identification of the whole range of linear and nonlinear mechanical properties of the tested sample. Only few attempts to perform time-dependent tests for the identifications of the nonlinear features of rubber bushings have been documented in the literature. For instance, Puel et al. [13] devised an adjoint state formulation of the identification problem, which demonstrated the feasibility of time-domain parameter identification. However, their study was limited to a time-identification performed using only a triangular periodic displacement at a rather limited speed. More recently, Rapp et al. [10] demonstrated that time-domain identification can be successfully used to accurately identify the dynamic response of bushing components. However, they proposed a rather complex hybrid method relying on a genetic algorithm within a particle-swarm-optimisation routine, which has quite a relevant impact on the computational burden and the overall applicability of the proposed approach.

This paper proposes a cost-effective time-domain system identification approach tailored to bushing components, which is based on two fundamental ideas. The first one relies on fitting the designated overlay model directly on the time-histories of the measured data, which is crucial to overcome the limitations of the procedures currently available. The second one relies on a time-domain methodology, which relaxes the assumptions of perfect steady-state time-harmonic response, thereby enhancing the robustness of the resulting identification process. This identification approach is expected to be of particular value in scenarios where non-linearity effects may distort significantly the shape of the bushing axial stress vs. axial strain hysteretic curve, which may even display multiple curls [14]. In real-world applications, bushing models should work under, and adjust to, a wide range of operational conditions. This study shows that, transient phenomena, which are normally overlooked in the current practice, should instead be used as a valuable resource to speed up the convergence of the identification process towards the most representative model parameters. These motivations have brought to the conception of the new system identification approach proposed in this paper, which relies on a single input signal characterised by a wide frequency band sweep with varying amplitude that has been specifically conceived to emphasise all the nonlinear phenomena that characterise the dynamic response of bushings.

To provide a detailed account of the proposed time-domain system identification procedure, the paper is structured in 5 sections. Section 2 describes the tested bushing sample, the experimental equipment and the overlay modelling strategy used to investigate the dynamic response of the bushing. Section 3 is focused on the model parameter identification. More specifically, it first recalls the classical DMA-based frequency-domain approach, which has been used to generate reference results. Then it details the proposed time-domain methodology. Finally the results of a set of identification exercises implemented with the newly proposed time-domain methodology are presented in Section 4, and then discussed in the closing Section 4.3 with respect to results obtained with the classical frequency-domain identification exercise.

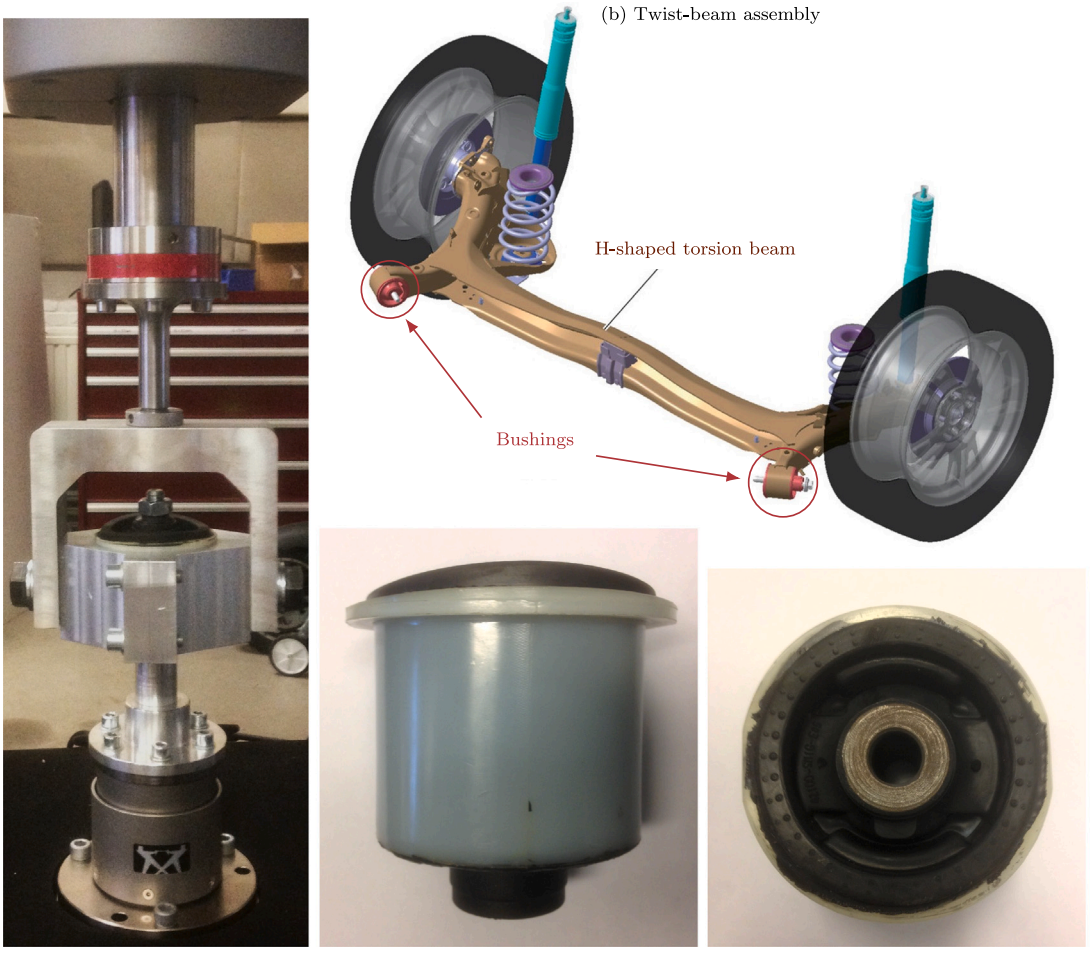

Fig. 1. Overview of the experimental Setup: (a) Bushing mounted on the apparatus; (b) schematic view of a Toyota Honda Civic rear twistbeam; (c) and (d), lateral and top view of the tested bushing sample.

2. Material and methods

To start with, this section describes in details the bushing sample and the test machine, which has been used to generate (a) the multiple time-harmonic tests at several frequencies and amplitudes for the classical system identification and (b) the single time-sweep test with varying amplitude for the proposed system identification. After that, it briefly revises the three lumped parameter models that have been used to identify the axial response of the bushing; namely, the classical Kelvin–Voigt, the Berg and the modified-Berg models.

2.1. Bushing sample

Fig. 1 shows the bushing that was tested and identified using the classical frequency-domain approach and the time-domain approach proposed in this study. The sample used in this work is part of the rear twist-beam suspension assembly (Fig. 1(b)) of a Toyota Honda Civic car model. The bushing is formed by three principal parts, namely a thin-walled outer cylinder made of steel, which contains a rubber ring with a hollowed steel pin at its interior. As can be seen in Fig. 1(b), the outer cylinder is housed on a special cylindrical seat made in the suspension structure. The internal pin is instead connected to the bodywork of the car via a bolt.

The dynamic response of the bushing is influenced significantly by this mounting configuration; in particular, the cylindrical seat has quite a relevant effect on the axial response of the bushing. Indeed, preparatory tests carried out upfront to this work showed that a free bushing sample would display quite a different axial stiffness than that of the actual bushing mounted on the structure of the car suspension and fixed onto the car bodywork.

2.2. Test setup and measurement protocol

The identification tests were run on the Instron E10000 electro-mechanical fatigue machine depicted in Fig. 1(a). To obtain the same functional behaviour of the bushing mounted on the car twistbeam suspension structure, a dedicated housing was designed and fabricated to mount the bushing on the fatigue machine. As can be noticed in Fig. 1(a), the ad-hoc casing was made of two hemi-cylindrical flanges that clamped the outer thin walled cylinder of the bushing in such a way as to replicate the cylindrical seat of the twist-beam suspension. The inner cylindrical pin of the bushing was fixed onto the machine moving piston with a bolt, making sure there would have been an accurate aligning of the bushing outer cylinder and inner pin axes.

The fatigue machine has a dynamic capacity of ± 10 kN, and a vertical stroke range of 60 mm. The machine is equipped with a load cell whose accuracy is rated at $\pm 0.5\%$ of the measured load, with a minimum value of ± 50 N. Lastly, the position accuracy is of the order of ± 0.001 mm. The machine with the specially dedicated clamp for the bushing sample at hand was used to produce both the steady-state time-harmonic measurements and the transient sweep measurements, respectively for the classical frequency-domain and for the newly proposed time-domain system identifications considered in this work.

Before performing any measurement, a set of preconditioning tests was executed in order to overcome the impact of the Mullins effect, which consists into a substantial softening of the material during the first few cycles of excitation [15]. The preconditioning was made by exciting the sample at very low speed, and with an amplitude 10% larger than the maximum one planned for the experimental campaign.

2.3. The overlay modelling approach

The system identification methodology proposed in this paper relies on the so-called overlay modelling approach. As discussed in [2], this approach exploits the superposition of independent physical effects, which are representative of the dynamic response of rubber-like materials, such as for example hyper-elasticity, visco-elasticity and internal-friction. Interested readers can find in [5] an exhaustive and updated review of the overlay modelling approach, including a library of the most common lumped-parameter branch models used in practice. Among all possible alternatives available in the literature (e.g. see Refs. [5,16]), the following three overlay models were considered in this study: (1) the Kelvin–Voigt model, (2) the Berg model and (3) a modified Berg variant. To keep the notation simple, over the remainder of the paper, they will be referred to as the KV model, the Berg model and the mod-Berg model respectively. In general, bushing components show quite a nonlinear dynamic response. Hence, it is expected that the KV model that encompasses solely a linear spring and a linear damper will not offer the best modelling option. Nevertheless, the KV model has been used to provide the basis for a comprehensive tutorial case study based on three models with incremental complexity. Hence, the identification study has been implemented starting from the simplest KV model to then move on to the Berg and modified Berg models that progressively exemplify the principal non-linear effects of bushings.

In principle a wider range of higher order models having more viscoelastic or Prandtl elements could have been taken into consideration too. However, to keep the analysis of the proposed time-identification approach simple, the study has been limited to the Berg and mod-Berg basic nonlinear models that, nevertheless, progressively cover the principal non-linear features of the bushing dynamic response. In this respect, it should be mentioned that a few more identification exercises had been run with higher order lumped parameter models, which, for the specific bushing at hand, showed marginal improvements on the prediction of its dynamic response.

The following subsections present a short overview of each model with respect to the physical quantities of interest both for the classical frequency-domain approach and for the newly proposed time-domain identification approach, which are respectively the frequency-dependent modulus of the Dynamic Stiffness, $K(\omega)$, and time-averaged Loss Energy, $W(\omega)$, and the restoring force, $F(t)$ (for simplicity in the remaining part of the paper $K(\omega)$ and $W(\omega)$ will be refereed to as the dynamic stiffness and the loss energy respectively). Assuming the time-harmonic relative displacement exerted on the bushing and the reactive force generated by the bushing are given by $x(t) = A(\omega)\cos(\omega t)$, $F(t) = F(\omega)\cos(\omega t + \phi(\omega))$, where ω is the circular frequency of the imposed vibration, $A(\omega)$ and $F(\omega)$ are respectively the real-valued amplitudes of the displacement and force and $\phi(\omega)$ is the phase lag between the imposed displacement and the reactive force, the modulus of the Dynamic Stiffness is given by

$$K(\omega) = \frac{F(\omega)}{A(\omega)} \tag{1}$$

whereas the time-averaged Loss Energy, which represents the energy absorbed by the bushing within a full cycle of vibration, is given by

$$W(\omega) = \oint F(t)dx = \int_0^{T=2\pi/\omega} F(t)\dot{x}(t)dt = \pi F(\omega)A(\omega)\sin\phi(\omega). \tag{2}$$

2.3.1. The Kelvin–Voigt (KV) bushing model

The KV model represents the simplest model for a bushing component, which, as shown in Fig. 2, is characterised by a linear spring and a linear damper in parallel.

The reactive force predicted by the KV model is a linear function of the imposed relative displacement, x, and relative velocity, $\dot{x}$, such that:

$$F(t, x, \dot{x}) = kx + c\dot{x}, \tag{3}$$

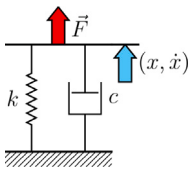

Fig. 2. The Kelvin–Voigt (KV) bushing model.

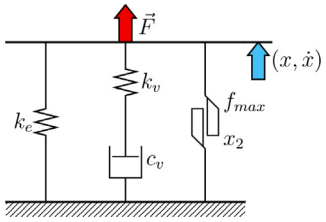

Fig. 3. Berg [16].

where k and c represent respectively the stiffness and damping coefficients of the spring and damper elements. The dynamic stiffness, K, and the loss energy, W, can be evaluated as functions of frequency and amplitude from Eqs. (1) and (2), which give:

$$K(\omega, A) = \sqrt{k^2 + \omega^2 c^2}, \tag{4}$$

$$W(\omega, A) = \pi \omega c A^2. \tag{5}$$

This model could be very effective in representing the equivalent dynamic stiffness behaviour of specific time-harmonic steady state working conditions. However, it is too simple when dealing with transient phenomena, spanning over multiple amplitudes and a broad range of frequencies.

2.3.2. The Berg model

When dealing with transient excitation characterised by a wide range of frequencies and encompassing a broad range of amplitudes, the KV model described in the previous section can be considered as a very simplistic option. Indeed, rubber filled compounds exhibit a characteristic stiffness decrement with respect to raising excitation amplitudes. This effect is known as the Payne effect [17,18], which can be effectively modelled with friction. In general, most friction models struggle to capture and represent in an effective and robust way the typical response of rubber like materials to time-varying excitation. Having considered all modelling options available in the literature (interested readers can find an in-depth analysis of non-linearity in rubber-like materials and the corresponding modelling options in [5,19]), the friction model proposed by Berg [16] was considered in this work, which suitably replicates the principal features of dynamic stiffness and loss energy in the bushing component under study. According to its original formulation [16], the Berg model depicted in Fig. 3 can be seen as an improved version of the classic Coulomb friction model, which encompasses purely elastic, viscous-elastic and, indeed, smooth Coulomb friction effects [20]. The model consists of three branches. There is a branch for the linear elastic effect, which is modelled with a spring of stiffness k_e. There is then a branch for the visco-elastic effect, which is modelled with a Maxwell-cell composed by a spring and damper in series having respectively stiffness k_v and damping c_v parameters. Finally there is a branch for the smooth Coulomb friction effect, which is modelled with a dedicated non-linear cell.

As depicted in Fig. 3, the overall reactive force of the Berg model is given by superposition of the linear elastic force effect, $F_e(x)$, the visco-elastic force effect, F_{ve}, and the friction force effect, $F_{fr}(x)$:

$$F(t, x, \dot{x}) = F_e(x) + F_{ve}(t, \dot{x}) + F_{fr}(t, x). \tag{6}$$

Here, the elastic component is simply given by

$$F_e(x) = k_e x. \tag{7}$$

Instead, the visco-elastic component, $F_{ve}(t, \dot{x})$ is typically governed by the following first order differential equation [5]:

$$\dot{F}_{ve}(t) = -\frac{k_v}{c_v} F_{ve}(t) + k_v \dot{x}, \tag{8}$$

which was integrated over time with a Runge–Kutta fourth-order scheme.

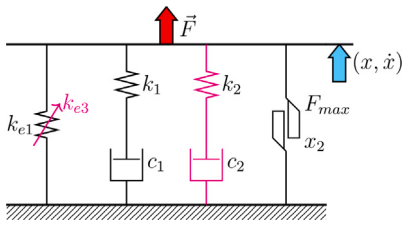

Fig. 4. Modified-Berg.

The friction component is modelled considering as internal states the reactive force, $F_s(t)$, and the relative displacement, $x_s(t)$, at each inversion of motion. Hence, according to [16], the friction force, F_{fr}, is evaluated as a function of the relative displacement, x, and its time-history with the following expressions:

$$F_{fr}(x) = \begin{cases} F_s + \dfrac{\Delta_s(x)}{x_2\left(1-\alpha_s\right)+\Delta_s(x)}\left(f_{max}-F_s\right), & x > x_s, \\ F_s, & x = x_s, \\ F_s + \dfrac{\Delta_s(x)}{x_2\left(1+\alpha_s\right)-\Delta_s(x)}\left(f_{max}+F_s\right), & x < x_s. \end{cases} \tag{9}$$

Here $\Delta_s(x) = x - x_s$, $\alpha_s = F_s/f_{max}$; and the parameter f_{max} represents the absolute value of the maximum friction force, whereas x_2 is the distance at which the resulting friction force would achieve half of the maximum value, when starting from resting conditions ($x_s = 0, F_s = 0$). The use of the internal states serves the purposes of holding a very compact representation of the axial stress–strain time-histories accumulated in the bushing. Considering time-harmonic vibrations, the dynamic stiffness, K, and loss energy, W, associated to the sole friction effect can be derived after a few mathematical steps with respect to the amplitude A of time-harmonic motion as follows [7,16]:

$$K_{fr}(A) = \alpha(A)\frac{f_{max}}{A} \tag{10}$$

$$W_{fr}(A) = 2f_{max}\left(2A - x_2\left(1+\alpha(A)\right)^2 \ln\frac{x_2\left(1+\alpha(A)\right)+2A}{x_2\left(1+\alpha(A)\right)}\right) \tag{11}$$

where

$$\alpha(A) = \left(\sqrt{{x_2}^2 + A^2 + 6x_2A} - x_2 - A\right)/\left(2x_2\right). \tag{12}$$

Here, it is worth noting that Eqs. (10) and (11) do not depend on frequency and, also, Eq. (9) does not depend on time.

Considering the formulation presented in [6] for time-harmonic motion, the dynamic stiffness, K, and loss energy, W, for the overall Berg model result given by:

$$K(\omega, A) = \sqrt{\left(k_e + k_{fr}(A) + k_v\omega/\Lambda_v\right)^2 + \left(k_v\Omega_v/\Lambda_v\right)^2} \tag{13}$$

$$W(\omega, A) = \pi k_v A^2 \omega\Omega_v/\Lambda_v^2 + W_{fr}(A) \tag{14}$$

where $\Omega_v = k_v/c_v$ and $\Lambda_v = \sqrt{\omega^2 + \Omega_v^2}$.

2.3.3. The modified Berg model

Although the Berg model covers the phenomenon of amplitude-dependent stiffness, in this study a modified Berg model was considered too. As depicted in Fig. 4, the mod-Berg model presents two new features with respect to its original version. Firstly, in place of the linear spring k_e, it adopts a cubic non-linear spring with linear and cubic coefficients k_{e1}, k_{e3}, which improves the description of the static and quasi-static elastic response. Secondly, to capture the visco-elastic effects over a wider frequency band, it encompasses two Maxwell-cells with stiffness and damping coefficients k_1, k_2, c_1, c_2 respectively.

The overall restoring force of the mod-Berg model is thus given by four components as follows:

$$F(t, x, \dot{x}) = F_{he}(x) + F_{ve}^1(t, \dot{x}) + F_{ve}^2(t, \dot{x}) + F_{fr}(t, x). \tag{15}$$

Here, the force exerted by the non-linear stiffness is given by the following odd cubic polynomial function:

$$F_{he}(x) = k_{e1}x + k_{e3}x^3, \tag{16}$$

where k_{e1} and k_{e3} are the linear and cubic stiffness coefficients. Also, as seen above for the Berg model, the visco-elastic forces are modelled in terms of the following two components

$$\dot{F}_{ve}^1(t) = -\frac{k_1}{c_1}F_{ve}^1(t) + k_1\dot{x}(t) \tag{17}$$

$$\dot{F}_{ve}^2(t) = -\frac{k_2}{c_2}F_{ve}^2(t) + k_2\dot{x}(t) \tag{18}$$

Table 1
Parameters used to compare the dynamic stiffness and loss energy of a model bushing element.

Branch type	Parameter	KC	Berg	mod-Berg	Units
Elastic	Linear Stiffness	$k = 60$	$k_e = 60$	$k_e = 60$	$[\frac{N}{mm}]$
	Cubic Stiffness			$k_e3 = -0.15$	$[\frac{N}{mm^3}]$
Viscous	Linear Damping	$c = 2.387$			$[\frac{N}{mm/s}]$
Elastic	1st Maxwell Cell Stiffness		$k_v = 60$	$k_1 = 30$	$[\frac{N}{mm}]$
	1st Maxwell Cell Damping		$c_v == 2.387$	$c_1 = 2.387$	$[\frac{N}{mm/s}]$
	2nd Maxwell Cell Stiffness			$k_2 = 30$	$[\frac{N}{mm}]$
	2nd Maxwell Cell Damping			$c_2 = 0.2387$	$[\frac{N}{mm/s}]$
Friction	Max Force		$f_{max} = 60$	$f_{max} = 60$	[N]
	Half Force Elongation		$x_2 = 0.25$	$x_2 = 0.25$	[mm]

where k_1, k_2 and c_1, c_2 are the stiffness and damping coefficients respectively for the two branches. Finally the friction effect is modelled with the expression given in Eq. (9) above. Here too, a Runge–Kutta fourth-order scheme was used to integrate Eqs. (17) and (18) over time. The effect of friction is formulated as in the original Berg model, thus using Eqs. (9), (10), and (11).

After a few mathematical steps, the dynamic stiffness, K, and loss energy, W, for the modified-Berg model can be derived in terms of the following two expressions:

$$K(\omega, A) = \sqrt{\begin{matrix}\left(k_{e1} + k_{e3}A^2 + k_{fr}(A) + \omega k_1/\Omega_1 + \omega k_2/\Omega_2\right)^2 + \\ + \left(k_1\Omega_1/\Lambda_1 + k_2\Omega_2/\Lambda_2\right)^2\end{matrix}}, \tag{19}$$

$$W(\omega, A) = W_{fr}(A) + \pi\omega A^2\left(\Omega_1 k_1/\Lambda_1^2 + \Omega_2 k_2/\Lambda_2^2\right) \tag{20}$$

where $\Omega_1 = k_1/c_1$, $\Omega_2 = k_2/c_2$; and $\Lambda_1 = \sqrt{\omega^2 + \Omega_1^2}$, $\Lambda_2 = \sqrt{\omega^2 + \Omega_2^2}$.

2.3.4. Comparative analysis

To provide more insights on the KV, Berg and mod-Berg lumped parameter models considered in this study, the spectra of the dynamic stiffness, $K(\omega)$, and loss energy, $W(\omega)$, produced by the three models are now investigated with respect to incremental amplitudes of the imposed stroke for a reference bushing.

The numerical analysis has been designed in such a way as to compare the principal features of the three models. In particular, the parameters listed in Table 1 have been chosen arbitrarily in such a way as the typical S-type transition of stiffness and bell-shaped peak of energy absorption occur at about 4 Hz and 40 Hz.

To start with, the left-hand side plots in Fig. 5 obtained from the KV model are considered. The solid line in the top plots shows that, at low frequencies, the dynamic stiffness is constant and it is controlled by the stiffness parameter k. After the cut-off frequency of about 4 Hz the effect of damping becomes more relevant and the dynamic stiffness tends to grow proportionally to frequency. According to Eq. (4), the cut-off frequency is given by the ratio $\omega_c = k/c$, thus it tends to higher values for materials with higher stiffness to damping ratio. As an example, the dashed line shows the dynamic stiffness for a material having two times higher stiffness. As one would expect for a linear material, the spectrum does not vary with respect to the amplitude of the imposed vibration. The solid lines in the bottom plot show that the spectrum of the energy loss generated by the viscous damping rises proportionally to frequency. Here, the energy absorption rises with the amplitude of the imposed vibration.

The spectra in the centre plots of Fig. 5 for the dynamic stiffness, $K(\omega)$, and loss energy, $W(\omega)$, generated with the Berg model are now investigated. Considering first the case of a low imposed vibration on the bushing, the lines in the top plot show a peculiar S-type spectrum where the dynamic stiffness shifts from a constant reference value to a higher value with a peculiar S-type transition at about 4 Hz. Considering now incrementally higher values of imposed strokes on the bushing, the S-type spectra are shifted progressively to lower values. In other words, the higher is the imposed vibration the lower tends to be the stiffness of the material. Moving to the loss energy plot, the spectrum for a low amplitude stroke depicted by the solid black line also shows a particular bell-shape, whose maximum occurs at about 4 Hz too. Hence, the energy dissipation is particularly effective at the transition frequency from the low to the high stiffness response of the bushing. When the amplitude of the stroke is augmented, the bell-shaped spectrum shifts to higher values and the amplitude of the bell-shape is progressively accentuated indicating an increasingly higher energy dissipation effect. Both the S-type spectrum of $K(\omega)$ and the bell-shape spectrum of $W(\omega)$ obtained from the Berg model encompass quite peculiar features, which are linked to the non-linear response of the bushing rubber material. As will be shown in the forthcoming sections of the paper, these features have been found in the measurements and parameter identification exercises carried out on the bushing sample described above.

To conclude, the spectra in the right-hand side plots of Fig. 5 for the dynamic stiffness, $K(\omega)$, and loss energy, $W(\omega)$, generated with the modified-Berg model are finally considered. Assuming a low imposed vibration on the bushing, the black line in the top plot shows a spectrum with the same transition from a low to a high stiffness encountered in the analysis of the Berg model. However,

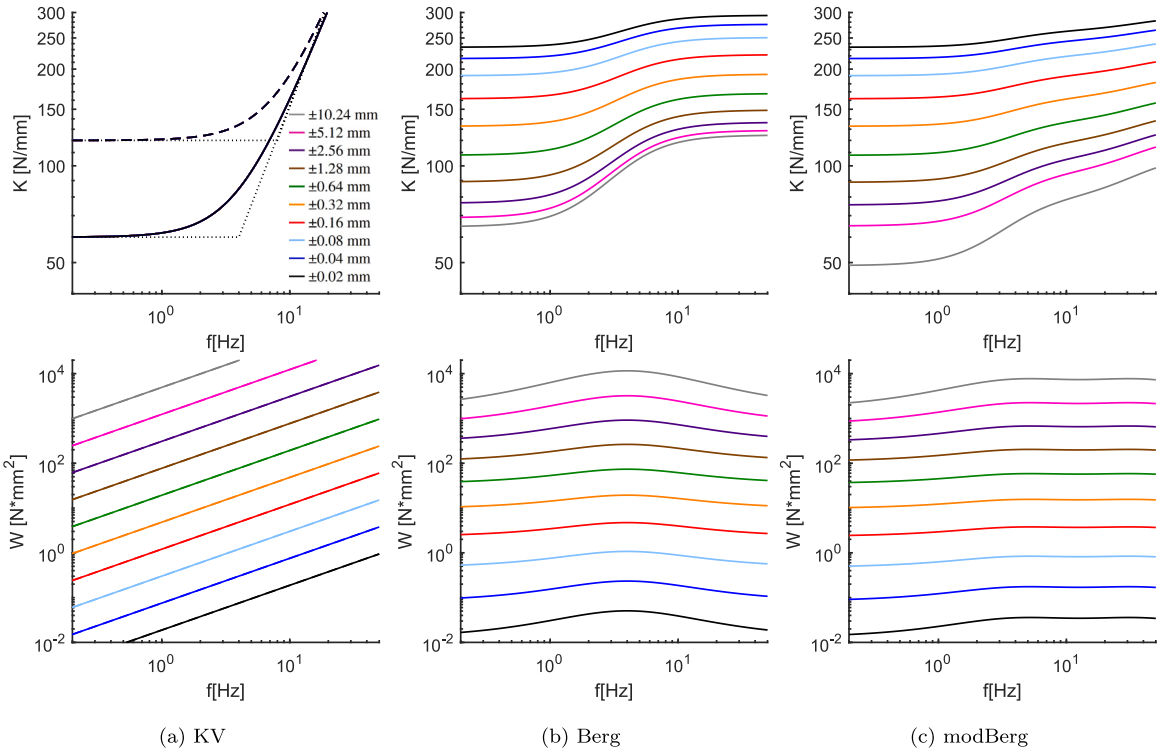

Fig. 5. Dynamic stiffness (top plots) and loss energy (bottom plots) curves for the (a) Kelvin–Voigt, (b) Berg, (c) Modified Berg models using the parameters listed in Table 1 for different values of the imposed stroke.

here the transition spans over a wider frequency band and it is characterised by a double S-type transition, one centred at about 4 Hz and the other at about 40 Hz. Again, the spectrum is shifted to lower values, that is the stiffness becomes smaller when the stroke exerted on the bushing is raised. A similar effect is noticed in the spectrum for the loss energy. In fact, there is now a wider bell-shape given by the superposition of two peaks centred at about 4 and 40 Hz respectively. The whole spectrum is raised when the amplitude of the imposed vibration on the bushing is brought up. As will be shown in the forthcoming sections these additional features were found at some extent on the measurements and identification exercises carried out on the bushing presented above.

3. Bushing parameter identification

As already stated in the introduction, this paper proposes a new time-domain system identification approach, which is assessed with respect to the classical frequency-domain procedure normally adopted to identify the dynamics of bushing components. Recalling the formulations presented in Section 2.3, and considering the frequency-domain and time-domain models employed in this study, the dynamic response of the bushing component can be described according to the following generalised parametric equation

$$B(q, \mathbf{p}) = f(q), \tag{21}$$

where $f(q)$ represents the physical parameter predicted by the model, which depends on given operation conditions q and, also, on the model parameters $\mathbf{p}$ that should be identified.

The bushing parameter identification can then be formalised with the following nonlinear data fitting problem:

$$\min_{\mathbf{p}} \sum_{i=1}^{N} \|f_i - B(q_i, \mathbf{p})\|^2, \tag{22}$$

which is posed by minimising, in a least-square sense, the differences between the measured f_i and predicted $B(q_i, \mathbf{p})$ physical quantity over a finite set $i = 1...N$ of operational conditions q_i, using the parameters $\mathbf{p}$ as the optimisation variables.

In this work, recursive gradient-based optimisation methods are employed to solve the nonlinear minimisation problems resulting from the classical frequency-domain and from the proposed time-domain formulations of the bushing parameter fitting with respect to the KV, Berg and mod-Berg lumped parameter models of the bushings. The method relies on the well-established *interior-point* approach, which is commonly used to efficiently solve nonlinear optimisation problems [21]. More specifically, the algorithm combines *line-search* and *trust-region* steps, as described in [22,23]. It is commercially available through the Matlab Optimization

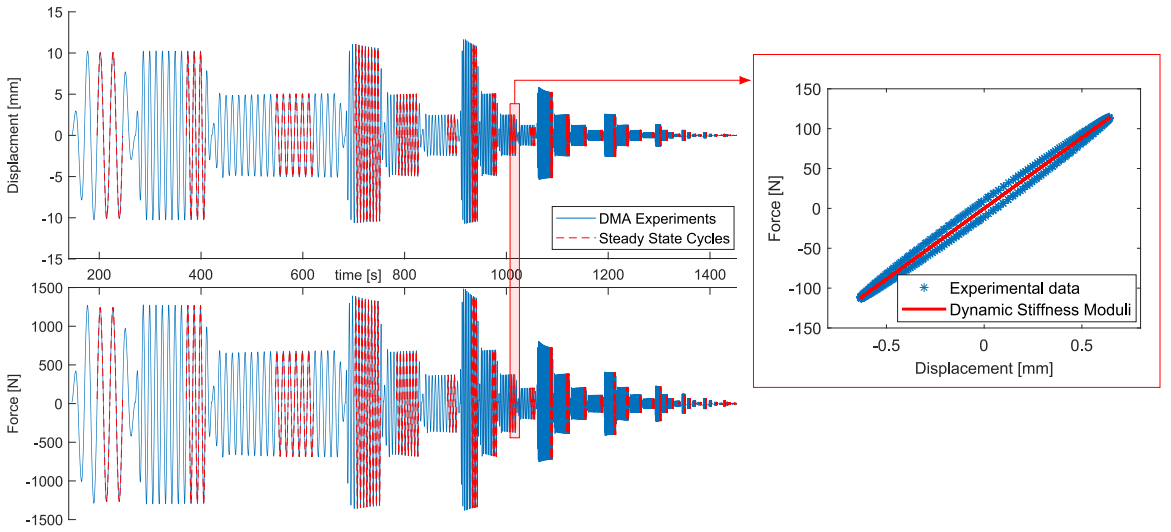

Fig. 6. DMA Tests Protocols: steady-state cycles are extracted from the whole testing sequence and processed separately in order to extract the dynamic stiffness parameters of the tested bushing, at several amplitude and frequencies.

Toolbox, in particular using the *lsqnonlin* function [24,25]. For completeness, the details of the formulations for both the classical frequency-domain and the proposed time-domain system identifications are reported in the following two subsections. In general, the multi-parameter optimisation exercise could lead to non-robust, or even non-physical, parameter values. Indeed, the optimisation could converge to excessively large or small parameters or even to negative, i.e. non-physical, parameters. Moreover, there is a danger that the optimisation can lock into local minima. For this reason, the optimisation was constrained in such a way as to limit the searched parameters within physically meaningful ranges. Moreover, to speed up the search of the optimal parameters, a multi-step parameterisation was implemented as suggested in [6,7].

3.1. Classical frequency-domain system identification: $FD-I$

Considering the classical frequency-domain system identification approach, the parametric model formulation given in Eq. (21), is specialised in terms of the dynamic stiffness $K(\omega, A)$ and loss energy $W(\omega, A)$ physical quantities, using the functions presented in Section 2.3 for the KV, Berg and mod-Berg models. The resulting frequency-domain parametric bushing model can be formalised as follows:

$$B^{FD}(\omega, A, \mathbf{p}) = \left\{ \begin{matrix} K(\omega, A) \\ W(\omega, A) \end{matrix} \right\}. \tag{23}$$

Here, the reference values of the dynamic stiffness $K(\omega, A)$ and loss energy $W(\omega, A)$ are extracted from a sequence of time-harmonic measurements taken for several combinations of frequencies and amplitudes. As a result, the problem in Eq. (22) is reformulated with the following weighted multi-objective minimisation:

$$\min_{\mathbf{p}} \sum_{i=1}^{N} \beta \left\| \frac{K_i^e - K(\omega_i, A_i)}{K_i^e} \right\|^2 + (1-\beta) \left\| \frac{W_i^e - W(\omega_i, A_i)}{W_i^e} \right\|^2. \tag{24}$$

In this expression, two misfit contributions are obtained considering the differences of the predicted dynamic stiffness, $K(\omega, A, \mathbf{p})$, and loss energy, $W(\omega, A, \mathbf{p})$, with their measured reference values, K_i^e and W_i^e, and then normalised with respect to the reference values themselves. Both contributions are linearly combined through the gain factor β, which weights the relative contributions of the dynamic stiffness and loss energy functions in the optimisation process. More specifically, when $0.5 < \beta < 1$ the optimisation is focused on the dynamic stiffness, whereas with $0 < \beta < 0.5$ it is directed more towards the loss energy.

3.1.1. Frequency-domain tests

As anticipated above, the frequency-domain identification relies on measurements of the dynamic stiffness and loss energy, K_i^e and W_i^e, which are used to fit the corresponding frequency and amplitude dependent parametric functions, $K(\omega, A, \mathbf{p})$ and $W(\omega, A, \mathbf{p})$, provided by the three bushing models. The reference measurement is generally retrieved from a sequence of steady-state time-harmonic tests taken at several frequencies and amplitudes.

Fig. 6 shows the whole time-history of the force and displacement measured in this study to perform the DMA-based frequency-domain identification. The measurement encompasses a sequence of time-harmonic tests characterised by 11 harmonics, spaced

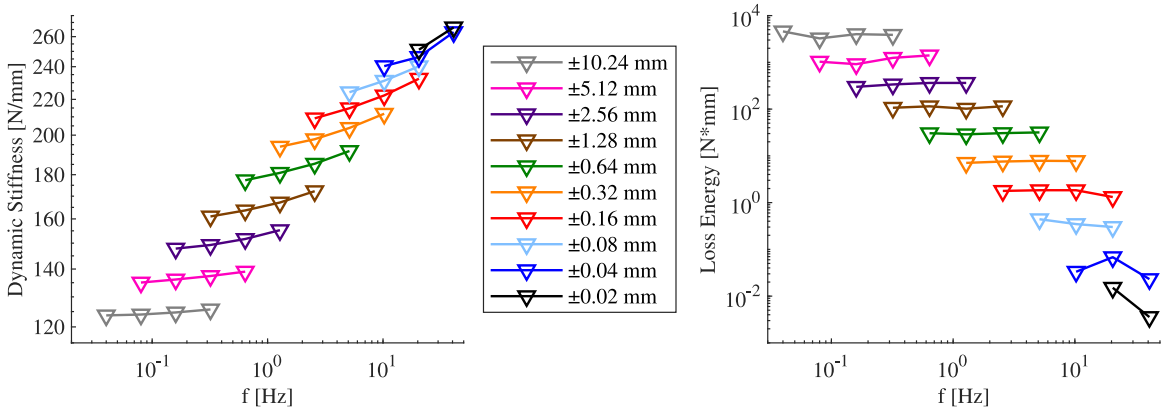

Fig. 7. Dynamic stiffness and Loss energy measured in DMA tests.

logarithmically between 0.04 Hz and 40 Hz, and a total of 10 amplitudes, comprised between 0.02 mm and 10.24 mm. Overall, a total of 35 time-harmonic tests were implemented in sequence.

The frequency-domain identification approach aims to extract the steady-state dynamic response; thus, as highlighted in red in Fig. 6, only the stationary portion of the measured signals was used for each frequency and amplitude. More specifically, for each steady-state section of the measurement, the Force vs. Displacement diagram shown on the right hand side of Fig. 6 was generated. Recalling the definitions given in Eqs. (1) and (2), the dynamic stiffness was calculated as the ratio between the amplitudes of the best-fitting force and displacement harmonic signals. Alternatively, it could have been retrieved from the slope of the principal axis of the quasi-elliptic hysteresis loop. Also, the loss energy was derived from the area of the hysteresis loop.

The two plots in Fig. 7 report the dynamic stiffness and loss energies extracted from the 35 time-harmonic tests carried out for this study. The graphs clearly show how the dynamic stiffness and the loss energy depend on the amplitude of the relative displacements imposed in the tests. In general, as found in Fig. 5, the dynamic stiffness tends to fall down as the amplitude of the displacement is raised whereas the energy loss tends to increase as the displacement is brought up. For given displacements, the dynamic stiffness tends to rise as the frequency is increased, particularly for small amplitude displacements. Instead, for each imposed displacement, the loss energy does not vary significantly with respect frequency.

In general, provided the measurement setup is properly installed, the DMA protocol does not suffer significantly from measurement noise effects, which, in any case, could be conveniently filtered out during the acquisitions or in the post processing phase of the measured force and displacement signals. However, it is quite vulnerable to non-ideal test conditions, in particular to non-perfectly steady state time-harmonic tests. To this end, a high precision test machine should be employed, which, moreover, should be carefully controlled in such a way as to ensure the acquired cycles have reached a full steady state time-harmonic condition, which allows derivation of neat force–displacement diagrams as those shown in Fig. 6, which are necessary to calculate accurately the dynamic stiffness (e.g. slope of the cycle) and the loss energy (e.g. area of the cycle).

3.2. Proposed time-domain system identification: $TD-I$

Moving to the proposed time-domain system identification, the parametric model given in Eq. (21), is specialised with respect to the reactive force $F(t,x,\dot{x})$ function defined in Section 2.3 for the KV, Berg and mod-Berg models :

$$B^{TD}(t,x,\dot{x},\mathbf{p}) = F(t,x,\dot{x}). \tag{25}$$

Here, the bushing samples were excited with a sigmoid-chirp relative displacement. Both the measured Force, $F^m(t)$, and the imposed relative displacement, $x(t)$, were then fitted in the KV, Berg and mod-Berg models.

In this case the minimisation of a least-squares misfit function was formulated with respect to the differences between the measured force, F_i^m, and the force predicted from the KV, Berg and mod-Berg models, $F(t_i,x_i^m,\dot{x}_i^m)$, at every time sample t_i, when using the measured motion, $(x^m,\dot{x}^m)$ as input to the bushing models:

$$\min_{\mathbf{p}} \sum_{i=1}^{N} (F_i^m - B^{TD}(t_i,x_i^m,\dot{x}_i^m,\mathbf{p}))^2. \tag{26}$$

3.2.1. Time-domain sigmoid-chirp test

The proposed-time domain approach relies on a single test where the reactive force produced by the bushing sample is measured with respect to an imposed relative displacement characterised by a sigmoid-chirp function, that is a sine function whose frequency is swept in a given range and whose amplitude is progressively lessened in such a way that the energy injected into the bushing is kept within the feasibility range of the machine.

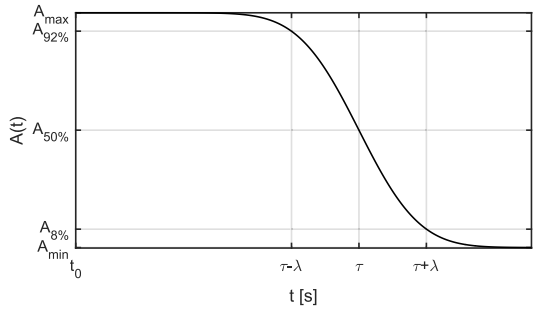

Fig. 8. The modulated amplitude (Eq. (28)) used for obtaining the sigmoid chirp signal.

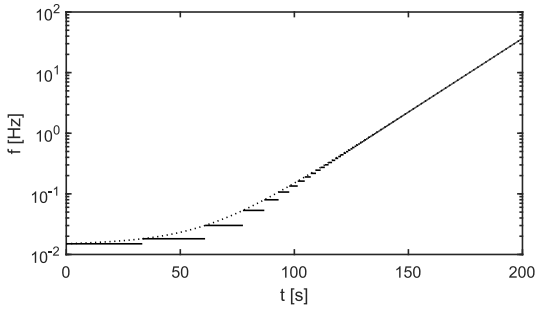

Fig. 9. The instantaneous frequency (Eq. (29)) used for obtaining the sigmoid chirp signal.

It is expected that, compared to the classical time-harmonic sequence of tests, this single test provides more accurate information on the non-linear response of the tested sample. To this end, the sigmoid-chirp function is selected in such a way as:

1. it excites the full range of motion in both compression and traction of the bushing sample;
2. it performs at least one full cycle at very low frequencies, such that friction effects can be captured, but without exciting viscous damping phenomena;
3. it covers the whole frequency bandwidth of interest;
4. it spans over the whole range of amplitudes of interest.

To comply with these requirements, the axial displacement imposed on the bushing sample should be characterised by a gentle chirp function with a smooth amplitude transition that lasts enough time such that the force response of the bushing sample covers both the frequency bandwidth and the amplitude range of interest. For instance, in this study the displacement imposed on the bushing was given by the following sigmoid-chirp function:

$$x(t) = A(t)sin\{\omega(t)t\}, \tag{27}$$

where, $\omega(t) = 2\pi f(t)$ and $A(t)$, $f(t)$ are the time-dependent amplitude and frequency of the sinusoidal function.

As depicted in Fig. 8, the proposed amplitude modulation function

$$A(t) = A_{min} + \frac{1}{2}\left(A_{max} - A_{min}\right) erfc\left(\frac{t-\tau}{\lambda}\right) \tag{28}$$

relies on the complementary error function, $erfc()$, which allows a sigmoid transition spanning from the maximum amplitude, A_{max}, to the lowest value, A_{min}. The τ delay represents the time shift computed from the centre of the transition zone, whereas the λ parameter is related to the slope of the transition.

Also, the modulation of the instantaneous frequency was modelled using the following relation:

$$f(t) = \frac{f_{max} - f_{min}}{sinh\left(F_r t_{max}\right)} sinh\left(F_r t\right) + f_{min}, \tag{29}$$

which guarantees a smooth transition starting from the f_{min} frequency, and reaching the f_{max} frequency at the t_{max} time, whereas the parameter F_r can be tuned to adjust the rate of frequency change. As depicted in Fig. 9, the frequency modulation was implemented in steps: the duration of each step was computed as the hemi-period corresponding to the instantaneous frequency evaluated using Eq. (29), $T_k = 0.5/f(t)$, at the beginning of each segment where the frequency was kept constant.

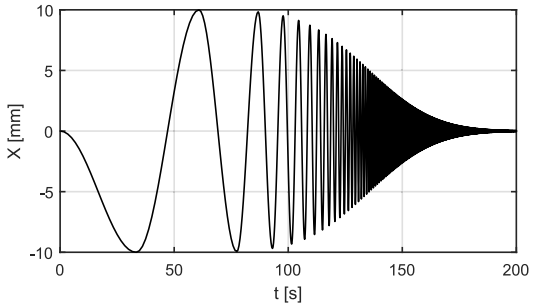

Fig. 10. The sigmoid-chirp signal.

Table 2
Sigmoid-chirp signal parameters.

A_{min}	0.02 [mm]	f_{min}	0.015 [Hz]
A_{max}	10 [mm]	f_{max}	40 [Hz]
τ	135.48 [s]	F_r	0.056 [Hz]
λ	32.26 [s]	t_{max}	200 [s]

Fig. 10 depicts the overall signal resulting from the combination of the frequency and amplitude profiles modulated according to Eqs. (28) and (29), using the parameters reported in Table 2.

In contrast to the DMA identification method, the proposed time-domain approach does not require the implementation of multiple time-harmonic cycles that must reach perfect steady state measurement conditions. On the contrary it simply requires the implementation of the sigmoid-chirp test depicted in Fig. 10. Here, the measured force and displacements signals can be used directly into the system identification algorithm, without the need of the signal post processing necessary to extract the time-harmonic response in the DMA approach. In general, the system identification converges to the right parameters of the model, even in presence of some deviations from the ideal sigmoid-chirp, provided the imposed displacement contains the relevant features of the sigmoid-chirp, that is the low to high frequency components with the imposed amplitude modulation. The presence of higher frequency components or the extension of the amplitude modulation to higher time windows will not significantly affect the identification. The most important requirement is that the displacement imposed onto the bushing contains full oscillations in the whole frequency range of the measurement, particularly at the lower end of the frequency range, and the higher frequencies are excited with a progressively lower amplitude. Higher frequency disturbances outside the range of the sigmoid chirp can nevertheless be conveniently filtered out during the acquisition or in the post processing phase of the system identification. The noise effects in the measured force are bound to be automatically mitigated in the optimisation algorithm for the identification of the system parameters.

4. System identification

As anticipated above, in this study, the axial dynamic response of the Honda twistbeam bushing sample described in Section 2.1 has been identified both with the classical frequency-domain procedure based on the DMA protocols and with the proposed time-domain approach. The two identification exercises were run with the fatigue machine described in Section 2.2 and depicted in Fig. 1(a). During each test, the strain displacement imposed on the bushing and the reactive force produced by the bushing were recorded. Then, the parameters in the KV, Berg and Mod-Berg models described in Section 2.3 were derived following the protocol of the classical frequency-domain identification recalled in Section 3.1 and the procedure of the proposed time-domain identification presented in Section 3.2. For the frequency-domain approach, a value of $\beta = 0.97$ was used. To assess and contrast the results of the two identification exercises, additional validation tests were implemented: two with pseudo-random excitation and the third with a Harmonic-Pulse imposed displacement.

4.1. Identification results

Table 3 reports the parameters identified with the classical frequency-domain and the proposed time-domain approaches for the KV, Berg and Mod-Berg models of the bushing axial response. At first sight, the parameters identified with the newly proposed time-domain approach seem to differ significantly from those obtained with the classical time-domain method. To better assess the impact of these differences, the Dynamic Stiffness, $K(\omega)$, and Loss Energy, $L(\omega)$, physical parameters have been derived with the Berg and Mod-Berg lumped parameter models presented in Sections 2.3.2, 2.3.3 using the parameters reported in Table 3 for the set of 10 excitation amplitudes implemented in the classical frequency domain identification exercise (e.g. see Fig. 7).

Figs. 11 and 12 show the Dynamic Stiffness and Loss Energy in the 0.04–40 Hz range derived respectively with the Berg and Mod-Berg lumped parameter models. The solid and dashed lines show the two functions calculated using the parameters derived

Table 3
Identification results.

Model variant and parameters		$DMA-I$	$TD-I$
KV	k[N/mm]	167.3	127.7
	c[Ns/mm]	0.167	0.591
Berg	k_1[N/mm]	107.9	120.2
	k_v[N/mm]	32.2	13.5
	c_v[Ns/mm]	0.57	4.06
	F_{fmax}[N]	206.8	64.08
	x_2[mm]	1.82	0.498
mod-Berg	k_{e1}[N/mm]	120.6	127.1
	k_{e3}[N/mm^3]	−0.056	−0.116
	k_1[N/mm]	10.341	6.285
	c_1[Ns/mm]	1.743	1.555
	k_2[N/mm]	26.429	20
	c_2[Ns/mm]	0.416	0.159
	F_{fmax}[N]	106.4	81.73
	x_2[mm]	1.082	0.766

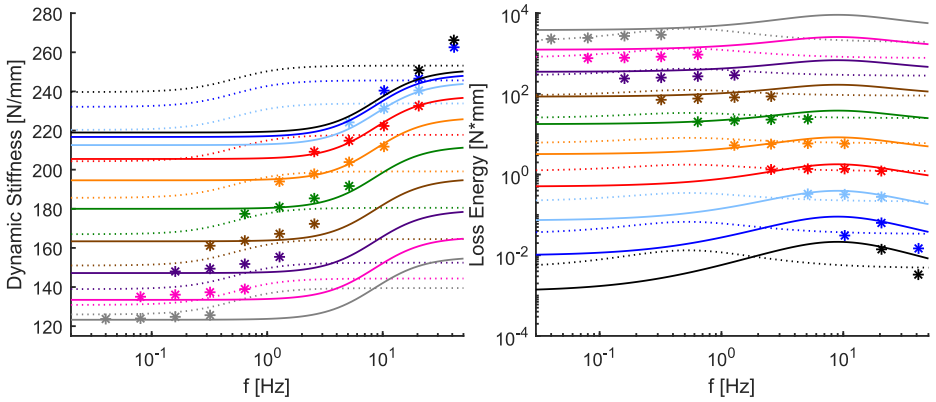

Fig. 11. Berg model evaluation in frequency-domain. ∗-markers depicts the experimental values. Solid curves represent the model obtained using the DMA-I approach; whereas dotted curve represents the model obtained by means of the TD-Ii approach.

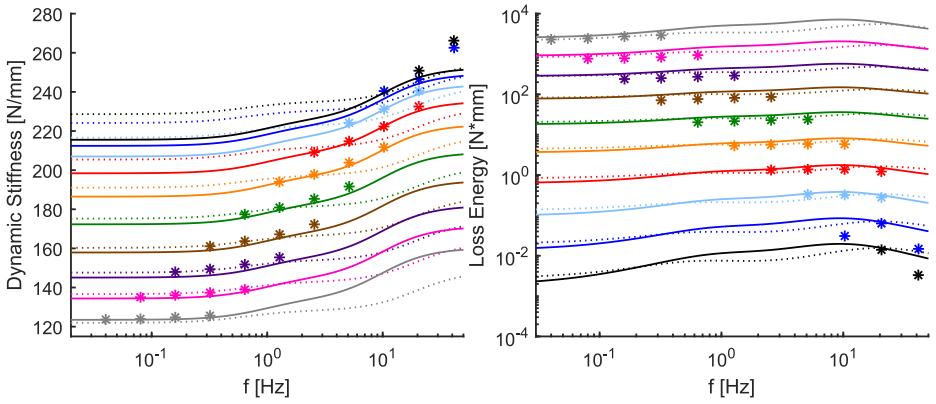

Fig. 12. mod-Berg evaluation in frequency-domain. ∗-markers depicts the experimental values. Solid curves represent the model obtained using the DMA-I approach; whereas dotted curve represents the model obtained by means of the TD-Ii approach.

from the classical frequency-domain and the proposed time-domain identification exercises respectively (second and third rows of Table 3). The values obtained directly from the time-harmonic measurements described in Section 3.1.1 are also plotted with the star markers. The curves for the Dynamic Stiffness $K(\omega)$ in the two Figures show a S-type transition between the constant-amplitude

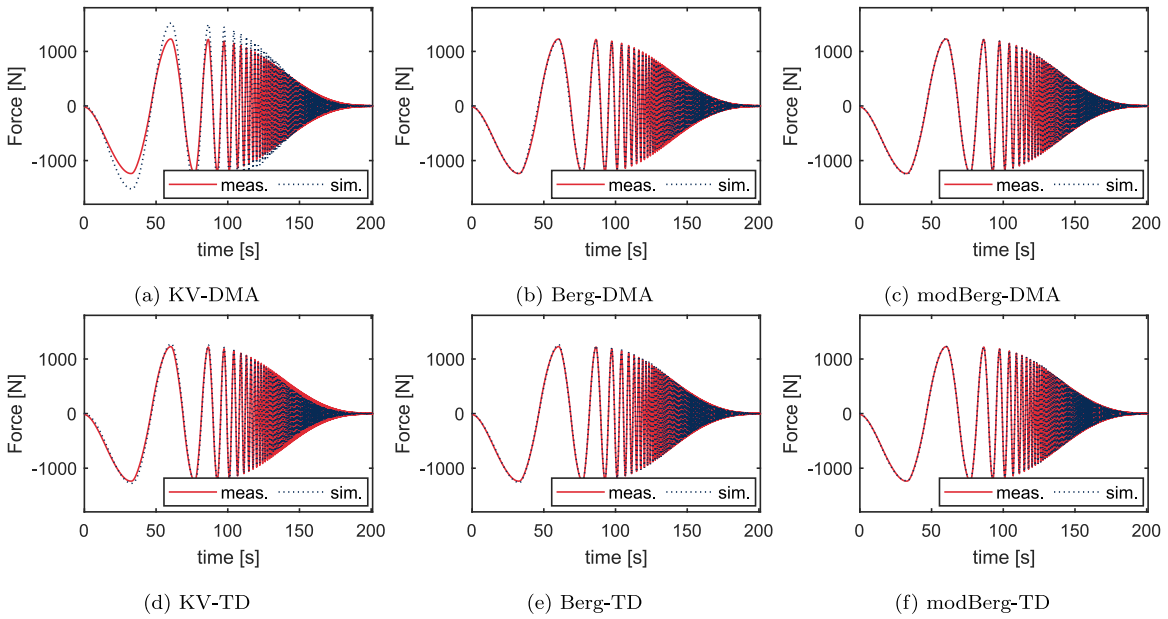

Fig. 13. Force evaluations for the sigmoid-chirp test.

asymptotes at low and high frequencies. Instead, the curves for the Loss Energy $L(\omega)$ show a smooth bell-shape, again with constant asymptotes at low and high frequencies.

Considering first the Dynamic Stiffness, in general, the curves predicted using the parameters identified with the time-domain approach are moved to higher values and their S-type section is centred at about 1 Hz. Instead the curves obtained from the parameters identified with the frequency-domain approach show comparatively lower values and their S-type section is centred around 10 Hz. Also, compared to the curves predicted with the Berg model, the curves derived from the Mod-Berg model are characterised by a smoother S-type transition between the low-frequency and high-frequency asymptotes. Overall, the time-domain identification leads to lower values of the Dynamic Stiffness with the S-type transition from the low to high frequencies asymptotes at lower frequency.

Moving to the Loss Energy, the curves derived from the parameters identified with the time-domain and frequency-domain approaches are about on equal levels of energy dissipation. Considering the results derived with the Berg model, the bell shapes of the curves calculated using the parameters obtained with the frequency-domain approach are shifted to significantly higher frequencies (about 10 Hz) than those derived from the parameters identified with the time-domain approach (about 0.5 Hz). Instead, the curves derived from the Mod-Berg model using either set of parameters are quite similar.

As one would expect, the dynamic stiffnesses and loss energies retrieved directly from the measurements (e.g. see Fig. 7), and displayed in Figs. 11 and 12 with stars, agree well with the simulations based on the parameters identified with the frequency-domain approach. However, if, as depicted in Fig. 13, the KV, Berg and mod-Berg models presented in Section 2.3 were used to reconstruct the reactive force produced by the samples during the time-domain tests with the imposed sigmoid-chirp displacements described in Section 3.2.1, then, as can be seen in Fig. 14, the errors between the measured reactive forces and those predicted with the parameters derived with the time-domain identification would be significantly lower than those between the measured reactive forces and those calculated from the parameters of the frequency-domain identification.

4.2. Identification performance assessment

To better evaluate the accuracy of the newly proposed time-domain identification method against that of the classical frequency-domain method, three tests were run, where, as shown in the top row of graphs of Fig. 15, the bushing sample was forced to vibrate under the two stationary random displacements and a transient harmonic pulse, which are shown on the top row of Figs. 15. The reactive force generated by the bushing to these displacements was measured and predicted with the KV, Berg and Mod-Berg models described in Section 2.3 using the parameters derived with both the classical frequency-domain identification and the newly proposed time-domain identification presented in Sections 3.1, 3.2 respectively. The graphs in the bottom row of Fig. 15 show the reactive forces measured for the three imposed displacements depicted on the top row of graphs.

The errors between the measured reactive forces and those reconstructed with the KV, Berg and mod-Berg models using the frequency and time domain identification approaches were then calculated and plotted in Figs. 16, 17, 18. Since the force signals oscillate around zero, the obtained errors were normalised with respect to the maximum absolute value of the measured reference forces.

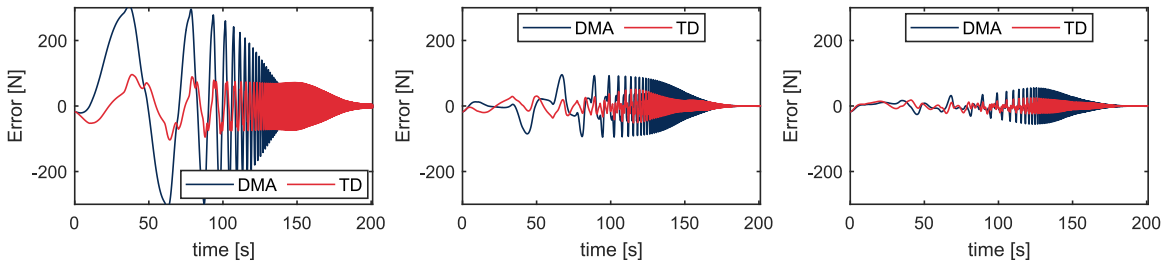

(a) KV (b) Berg (c) modBerg

Fig. 14. Errors evaluations in time-domain: DMA vs TD.

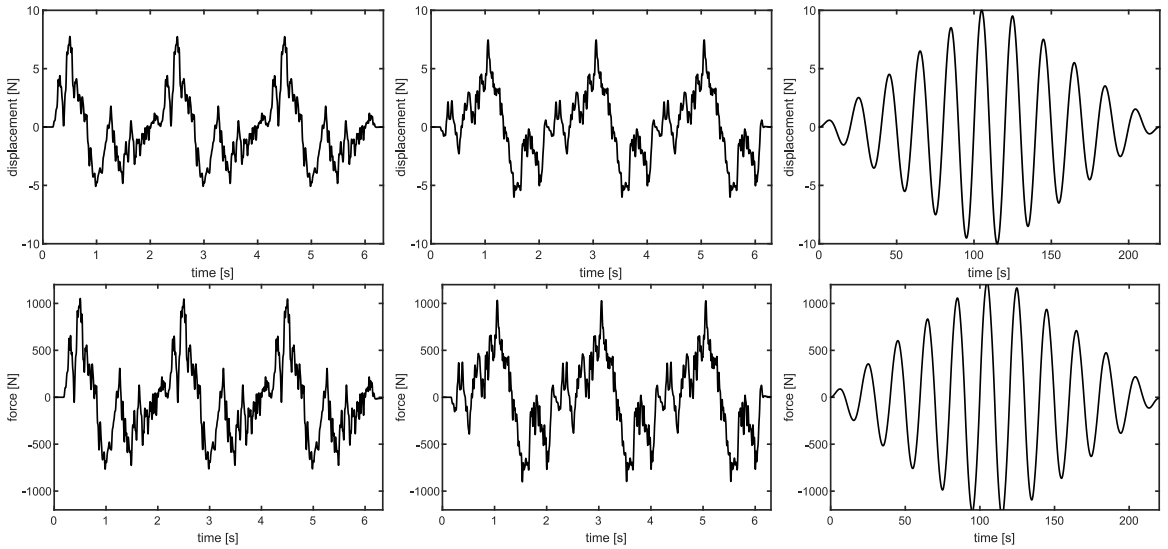

(a) random 1 (b) random 2 (c) Harmonic pulse

Fig. 15. Validation tests.

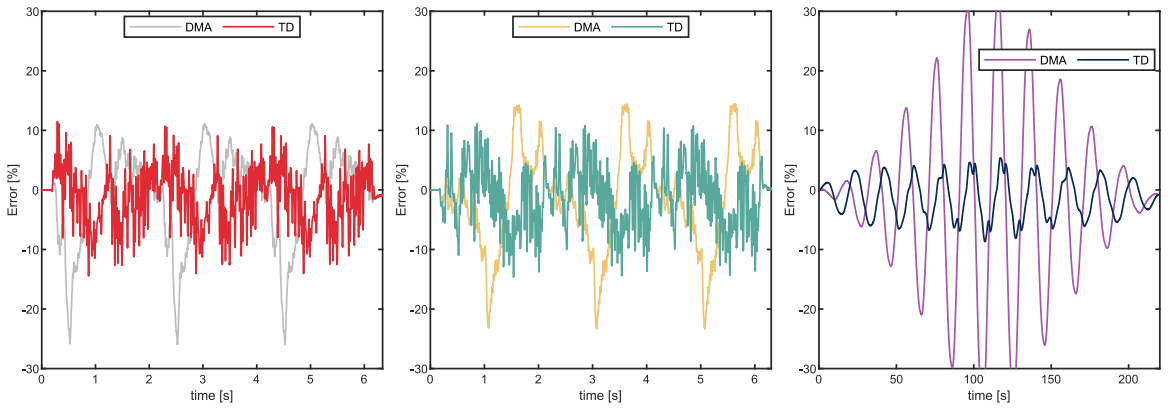

(a) random 1 (b) random 2 (c) harmonic pulse

Fig. 16. Errors of the KV models in validation tests.

Considering the case where the response of the bushing is predicted with the KV model, Fig. 16 shows that, when the bushing is excited by stationary-random displacements, the error between the measured and the predicted reactive forces based on the

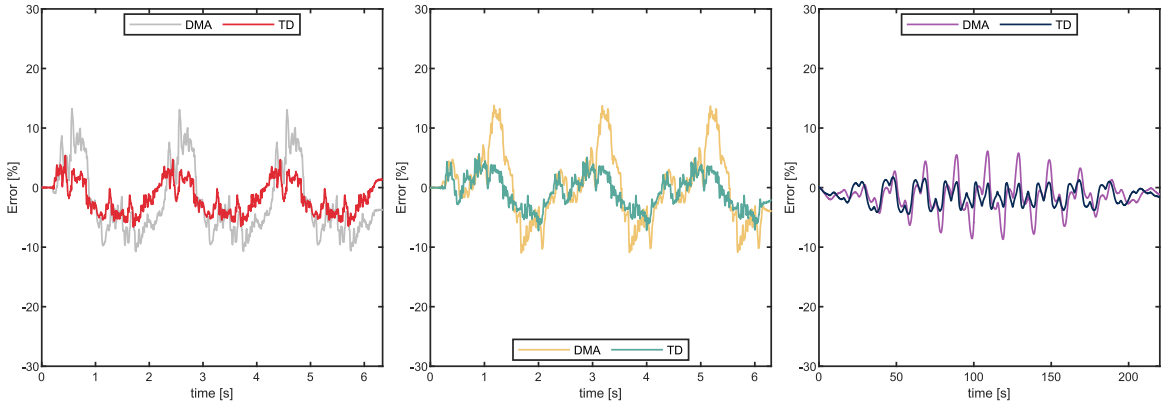

(a) random 1 (b) random 2 (c) harmonic pulse

Fig. 17. Errors of the Berg models in validation tests.

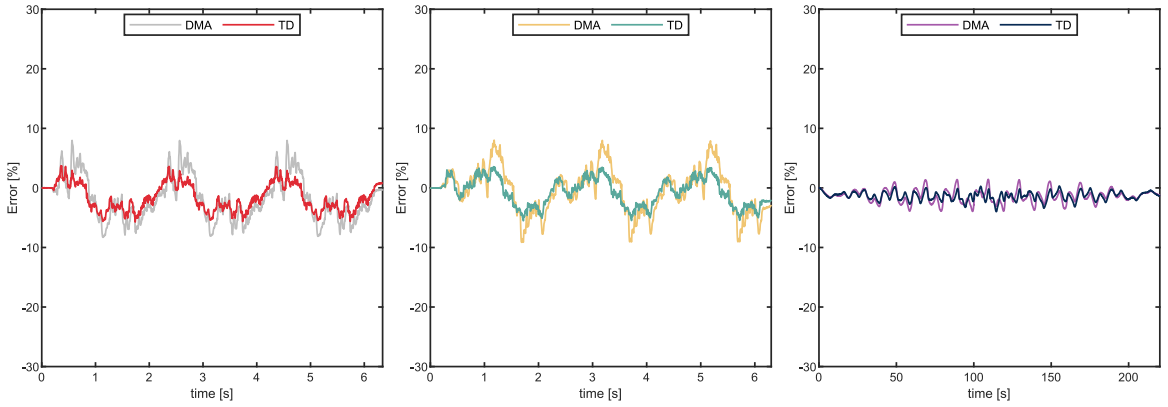

(a) random 1 (b) random 2 (c) Harmonic pulse

Fig. 18. Errors of the mod-Berg models in validation tests.

frequency-domain and time-domain identifications are similar. Instead, for the transient harmonic-pulse, the error is considerably smaller when the reactive force is predicted using the parameters identified with the time-domain approach. These results suggest that the proposed approach performs rather well in quasi-static transient conditions, even in the case where the basic KV model were used in the identification process.

When the Berg model is employed, as depicted in Fig. 17, smaller errors were reported for all types of excitation, with a significant improvement for the transient pulse, which was, nevertheless, expected with the more advanced Berg model. It is worth noting that, the predictions based on the time-domain identification lead to smaller errors than those based on the frequency-domain identification for both the stationary-random and the transient-harmonic imposed displacements.

Finally, when the reactive force produced by bushing is predicted with the mod-Berg model, Fig. 18 shows a further decrement of the errors for all types of excitation. Moreover, the predictions based on the parameters identified with either the time-domain or the frequency-domain approaches are qualitatively similar.

The outcomes from these performance tests confirm that, as reported in recent studies available in the literature [10,13], the proposed time-domain approach can lead to more accurate, as well as faster and simpler, identification exercises. The results presented in this study indicate that the time-domain identification may lead to better prediction of the bushing force, when using simpler models, such as the Berg and KV models. Instead, in case of more complex models, such as the mod-Berg model considered in this study, the proposed identification approach provides comparatively similar level of accuracy as that obtained with the canonical frequency-based identifications.

From a numerical perspective, both methods require very short computing time compared to the time necessary to implement the measurements. For instance, the algorithm for the frequency-domain identification required 5, 7, and 12 iterations to complete the optimisations for the KV, Berg and Mod-Berg models, which resulted in about 7, 10, and 20 ms of computation time respectively. Instead, for the time-domain approach, the optimisations for the KV, Berg and Mod-Berg models required 3, 60 and 61 iterations

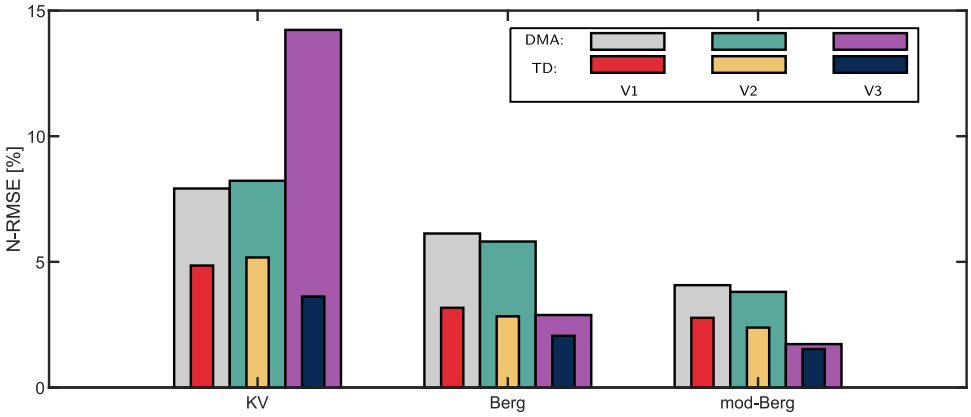

Fig. 19. Comparative results.

to converge, that is about 0.3, 29, and 61 s of computation time. Nevertheless, the set of measurements taken for the frequency domain approach took about 30 min, whereas the measurements for the time-domain method required only 3 min.

4.3. Frequency-domain vs time-domain identifications

To provide a more concise and effective analysis of the results presented in this paper, the normalised root mean square errors(NRMSE) between the measured and predicted reactive forces generated by the bushing in response to the displacements considered in this paper are reported in Fig. 19. Each bar in the plot corresponds to the NRMSE of the signals reported in Figs. 16, 17, and 18, for the identifications derived from the KV, Berg and Mod-Berg models respectively. Three validation cases (indicated as $V1$, $V2$, and $V3$ in the legend) where considered, for a total of nine comparisons: three for each model. The performance, in terms of NRMSE is reported for both the classical frequency-domain approach (thick bars) and the newly proposed time-domain method (thin bars).

In general this bar plot indicates that increasing the model complexity leads to better predictions of the dynamic response of the bushing. More specifically, a substantial improvement is obtained when the KV model is upgraded to the Berg model, especially in terms of accuracy of predicting the transient response to the harmonic pulse test. Indeed, the addition of the nonlinear stiffness and the friction damping effects was crucial to increase the accuracy of the prediction and identification too. The adoption of the second Maxwell-cell into the modified Berg model produced even further improvements of both the response prediction and parameters identification.

Contrasting the thick and thin bars in the three sets of results it can also be concluded that, in general, the proposed time-domain system identification leads to more accurate predictions of the bushing response than the classical frequency-domain identification, particularly when the simple KV model is employed.

5. Conclusions

This paper has proposed a time-domain methodology for the identification of lumped parameter models for the dynamic response of bushing components. The method relies on a single test, where the bushing is excited axially with a sigmoid-chirp displacement function. Such imposed displacement function is designed to specifically excite all the nonlinear transient phenomena typical of elastomers such as the bushing considered in this paper. The proposed time domain approach greatly simplifies the identification procedures, which are carried out without post-processing and without the need of driving the machines with stationary harmonic excitations. Moreover, it allows the implementation of a canonical nonlinear least-squares optimisation to fit on the measured data the lumped parameter models normally used to describe the nonlinear response of bushing components.

The proposed identification methodology was investigated with respect to three lumped parameters models of the bushing; namely: the Kelvin–Voigt model, the Berg model and the modified-Berg model. The accuracy of the proposed time-domain identification was assessed with respect to the classical frequency domain identification considering three tests where the bushing was excited axially with an imposed displacement: two cases with a periodic random signal and a third one with a transient harmonic pulse. More specifically, the reaction force produced by the bushing to these displacement functions was recorded and contrasted with the forces predicted with the three models using the parameters identified with both the proposed time-domain approach and the classical frequency-domain method.

In all cases, the time-domain approach lead to an accuracy improvement of at least 25%, while reducing the measurement campaign time from about 1500 s of the DMA tests to just 200 s, with a relative reduction of about 86%. Overall, the proposed time-domain approach does not solely reduce the testing time, but it also provides more accurate parameters, which in turn lead to more precise models for the prediction of the time-domain dynamic response of bushings.

CRediT authorship contribution statement

Francesco Cosco: Writing – review & editing, Writing – original draft, Visualization, Validation, Supervision, Software, Resources, Project administration, Methodology, Investigation, Formal analysis, Data curation, Conceptualization. **Lorenzo Della Siega:** Writing – original draft, Software, Methodology, Investigation, Formal analysis, Data curation, Conceptualization. **Rocco Adduci:** Writing – review & editing, Software, Resources, Methodology, Investigation, Data curation. **Paolo Gardonio:** Writing – review & editing, Writing – original draft, Conceptualization. **Wim Desmet:** Writing – original draft, Resources, Project administration, Funding acquisition. **Domenico Mundo:** Writing – review & editing, Project administration, Funding acquisition.

Declaration of competing interest

The authors declare that they have no known competing financial interests or personal relationships that could have appeared to influence the work reported in this paper.

Acknowledgements

This research was partially funded by the European Union through the European Social Fund (FSE) under the REcovery Assistance for Cohesion and the Territories of Europe (REACT-EU) initiative, within the context of the National Operational Programme (PON) on Research and Innovation 2014–2020, pursuant to DM 1062/2021, CUP H25F21001220006.

Data availability

Data will be made available on request.

References

[1] J.H. Sohn, S.K. Lee, J.K. Ok, W.S. Yoo, Comparison of semi-physical and black-box bushing model for vehicle dynamics simulation, J. Mech. Sci. Technol. 21 (2007) 264–271, http://dx.doi.org/10.1007/BF02916287.
[2] P.E. Austrell, Modeling of Elasticity and Damping for Filled Elastomers (M.D. dissertation), Structural Mechanics, Lund University, 1997.
[3] F. Karlsson, P. Anders, Modelling Non-linear Dynamics of Rubber Bushings: Parameter Identification and Validation (M.D. dissertation), Lund University, 2003.
[4] J. Ok, W. Yoo, J. Sohn, Experimental study on the bushing characteristics under several excitation inputs for bushing modeling, Int. J. Automot. Technol. 8 (4) (2007) 455–465.
[5] R. Adduci, M. Vermaut, M. Perrelli, F. Cosco, S. Vanpaemel, F. Naets, D. Mundo, A review of bushing modelling approaches for multibody simulations, Mech. Mach. Theory 191 (2024) 105496, http://dx.doi.org/10.1016/J.MECHMACHTHEORY.2023.105496.
[6] S.D. Kai Sedlaczek, J. Rauh, Advanced modular modelling of rubber bushings for vehicle simulations, Veh. Syst. Dyn. 49 (5) (2011) 741–759, http://dx.doi.org/10.1080/00423111003739806.
[7] F. Cosco, G. Gatti, A. Toso, S. Donders, D. Mundo, An optimized identification method for modular models of rubber bushings, in: RASD 2013 11th International Conference on Recent Advances in Structural Dynamics 1st–3rd July 2013, 2013.
[8] C.F. Yang, Z.H. Yin, W.B. Shangguan, X.C. Duan, A study on the dynamic performance for hydraulically damped rubber bushings with multiple inertia tracks and orifices: Parameter identification and modeling, Shock Vib. (2016) http://dx.doi.org/10.1155/2016/3695950.
[9] S. Dzierżek, Experiment-based modeling of cylindrical rubber bushings for the simulation of wheel suspension dynamic behavior, SAE Trans. (2000) 78–85, http://dx.doi.org/10.4271/2000-01-0095.
[10] T. Rapp, G. Jacobs, J. Berroth, R. Bauermeister, S. Wischmann, Optimization workflow to parameterize elastomer material models based on arbitrary time-domain measurement data, J. Appl. Polym. Sci. 140 (2023) http://dx.doi.org/10.1002/app.53974.
[11] G. Li, L. Wu, S. Zhang, F. Liu, Frequency dependence prediction and parameter identification of rubber bushing, Sci. Rep. 12 (1) (2022) 863, http://dx.doi.org/10.1038/s41598-022-04839-2.
[12] Z. Zhang, H.H. Zhang, Viscoelastic parameter identification based structure-thermal analysis of rubber bushing, Glob. J. Res. Eng. (2014).
[13] G. Puel, B. Bourgeteau, D. Aubry, Parameter identification of nonlinear time-dependent rubber bushings models towards their integration in multibody simulations of a vehicle chassis, Mech. Syst. Signal Process. 36 (2) (2013) 354–369, http://dx.doi.org/10.1016/j.ymssp.2012.10.021.
[14] H.J. Pain, The Physics of Vibrations and Waves, John Wiley and Sons Inc, 2005.
[15] L. Mullins, Softening of rubber by deformation, Rubber Chem. Technol. 42 (1) (1969) 339–362, http://dx.doi.org/10.5254/1.3539210.
[16] M. Berg, A non-linear rubber spring model for rail vehicle dynamics analysis, Veh. Syst. Dyn. 30 (1998) 197–212, http://dx.doi.org/10.1080/00423119808969447.
[17] A.R. Payne, The dynamic properties of carbon black-loaded natural rubber vulcanizates. Part I, J. Appl. Polym. Sci. 6 (19) (1962) 57–63, http://dx.doi.org/10.5254/1.3539570.
[18] R. Hentschke, The Payne effect revisited, Express Polym. Lett. 11 (4) (2017) http://dx.doi.org/10.3144/expresspolymlett.2017.28.
[19] X. Feng, P. Xu, Y. Zhang, Filled rubber isolator's constitutive model and application to vehicle multi-body system simulation: a literature review, SAE Int. J. Veh. Dyn. Stab. and NVH 2 (2018) 101–120, http://dx.doi.org/10.4271/10-02-02-0007.
[20] E. Pennestrì, V. Rossi, P. Salvini, P.P. Valentini, Review and comparison of dry friction force models, Nonlinear Dyn. 83 (2016) 1785–1801, http://dx.doi.org/10.1007/s11071-015-2485-3.
[21] I. Pólik, T. Terlaky, Interior point methods for nonlinear optimization, in: Nonlinear Optimization, Springer, 2010, pp. 215–276, http://dx.doi.org/10.1007/978-3-642-11339-0_4.
[22] R.H. Byrd, J.C. Gilbert, J. Nocedal, A trust region method based on interior point techniques for nonlinear programming, Math. Program. 89 (1) (2000) 149–185, http://dx.doi.org/10.1007/PL00011391.
[23] R.A. Waltz, J.L. Morales, J. Nocedal, D. Orban, An interior algorithm for nonlinear optimization that combines line search and trust region steps, Math. Program. 107 (3) (2006) 391–408, http://dx.doi.org/10.1007/s10107-004-0560-5.
[24] T.F. Coleman, Y. Li, On the convergence of interior-reflective Newton methods for nonlinear minimization subject to bounds, Math. Program. 67 (1–3) (1994) 189–224, http://dx.doi.org/10.1007/BF01582221.
[25] T.F. Coleman, Y. Li, An interior trust region approach for nonlinear minimization subject to bounds, SIAM J. Optim. 6 (2) (1996) 418–445, http://dx.doi.org/10.1137/0806023.